

Dual-Gate Organic Electrochemical Transistors for Marine Sensing

Shuo-En Wu, Lulu Yao, Alan Shiller, Andrew H. Barnard, Jason David Azoulay, and Tse Nga Ng*

Monitoring dissolved oxygen is essential to marine research, but the high redox potentials required to drive sensing reactions have posed an ongoing instability issue in the sensors. Here, a novel dual-gate configuration for organic electrochemical transistors that extends the device electrochemical stability window is demonstrated. This paper presents the sensor operating principle that relates the channel conductance to potentials on the two gates. This broadly applicable design allows a large potential to be applied between the gates for sensing analytes, while synergistically modulating the channel within a lower potential range to maintain the stability of the semiconductor. Specifically, the sensor achieves a detection limit of 0.3 ppm dissolved oxygen concentration in seawater, with a sensitivity of 222 μ A cm⁻² ppm⁻¹ for concentrations below 5 ppm. The device demonstrates reliable operation over 5 days and is capable of monitoring oxygenation changes arising from the photosynthesis cycles of saltwater macro-algae. This dual-gate configuration serves to extend the sensor operating voltage window and improves device stability. Thus, this new configuration provides a new type of compact, robust sensor for marine research, and opportunities in other fields ranging from wastewater management to bioelectronics.

S.-E. Wu, L. Yao, Prof. T. N. Ng Materials Science Engineering Program University of California San Diego La Jolla, CA 92093, USA E-mail: tnn046@ucsd.edu Prof. A. Shiller Division of Marine Science University of Southern Mississippi Stennis Space Center, MS 39529, USA Dr. A. H. Barnard Sea-Bird Scientific 620 Applegate Street, Philomath, OR 97370, USA Prof. J. D. Azoulay School of Polymer Science and Engineering The University of Southern Mississippi Hattiesburg, MS 39406, USA Prof. T. N. Ng Department of Electrical and Computer Engineering University of California San Diego La Jolla, CA 92093, USA

The ORCID identification number(s) for the author(s) of this article can be found under https://doi.org/10.1002/aelm.202100223.

DOI: 10.1002/aelm.202100223

1. Introduction

The marine ecosystem is experiencing significant anthropogenic-driven changes. Rising temperatures decrease the solubility of oxygen in water, and less dissolved oxygen has devastating impacts on aquatic life, aquaculture, marine environments, and biodiversity.[1] To assess and manage stressors that exacerbate deoxygenation, there is an urgent need for the development of compact, economical sensor technologies that facilitate widespread in situ monitoring of oxygen in the marine environment. Compared to conventional bulky probes,^[2] thin-film sensors^[3-6] can lead to reductions in size, weight, and cost that enable nonintrusive monitoring systems. For example, miniaturized sensors can be placed in new locations, such as inside crevices in coral reefs to study the urgent problem of reef bleaching, or integrated as electronic tags on marine creatures to monitor environmental variables in their surroundings.^[7] In particular, organic electrochemical transistors (OECTs) offer

the advantages of inherent signal amplification^[8] and biocompatibility.^[9] Upon incorporation of redox receptors or selective membranes, OECTs demonstrate sensitive detection of specific metabolites^[10-13] and ions^[14,15] in aqueous media and are desirable as miniaturized marine sensors. However, for analytes with high redox potentials such as dissolved oxygen, [16] the large voltage required to drive the sensing reaction may inherently alter the chemical composition of the semiconductor within the OECT channel and degrade device performance.[17,18]

The instability of OECTs in the presence of the oxygen reduction reactions (ORRs) has been an ongoing challenge, and recent research has modified the semiconducting polymers to shift the operational voltage window^[18-20] and minimize ORRs at the channel. While promising, new polymers have yet to match the performance of poly(3,4-ethylenedioxythiophene): polystyrene sulfonate (PEDOT:PSS), the most commonly used semiconductor in state-of-the-art OECTs. Here, we extend the OECT electrochemical stability window by using a new device configuration, which is broadly applicable to all semiconducting polymers including PEDOT:PSS. Typical OECTs have three electrodes (gate, source, and drain), in which either the source or drain electrode serves as the ground reference point. Our OECT design adds a fourth electrode to serve as the ground,



allowing both source and drain electrode potentials to be tuned to avoid undesirable over-oxidization at the OECT channel. This new configuration permits a high potential to be applied between the gate and the fourth electrode (reference gate) to induce sensing reactions; then the channel conductance is proportionately modulated at lower potentials to maintain semiconductor stability. Thus, the new dual-gate OECT structure can accommodate high-potential reactions such as ORRs at the gates, while it does not subject the channel to high potentials that cause degradation.

Specifically, this work shows that dual-gate OECTs are highly sensitive and stable for monitoring dissolved oxygen concentration in seawater, a highly challenging matrix owing to its high ionic strength and multitude of chemical interferents. We present the sensor operating principle, by deriving the channel conductance with respect to potentials on the two gates. In addition to oxygen, this modulation principle is generalizable to other analytes with high redox potentials such as nitrates and dissolved carbon dioxide. Here, the dual-gate OECT was used in

an in situ sensing demonstration to track oxygen release from the photosynthesis cycles of saltwater macro-algae, [21,22] demonstrating its high sensitivity. The results demonstrate that our new OECT configuration can extend the sensor operating voltage window and improve the device stability, to provide a new class of compact, robust sensors for marine research, and other fields ranging from waste-water management to bioelectronics.

2. Results and Discussion

2.1. Channel Modulation Principles in Dual-Gate OECTs

The structure of a conventional three-electrode OECT is shown in **Figure 1**a. The channel semiconductor was PEDOT:PSS etched by sulfuric acid, and the acid treatment removed PSS to form PEDOT films with improved conductivity and stability.^[23–25] A gel electrolyte consisting of xanthan gum^[26] with sodium sulfate was deposited onto the OECT channel

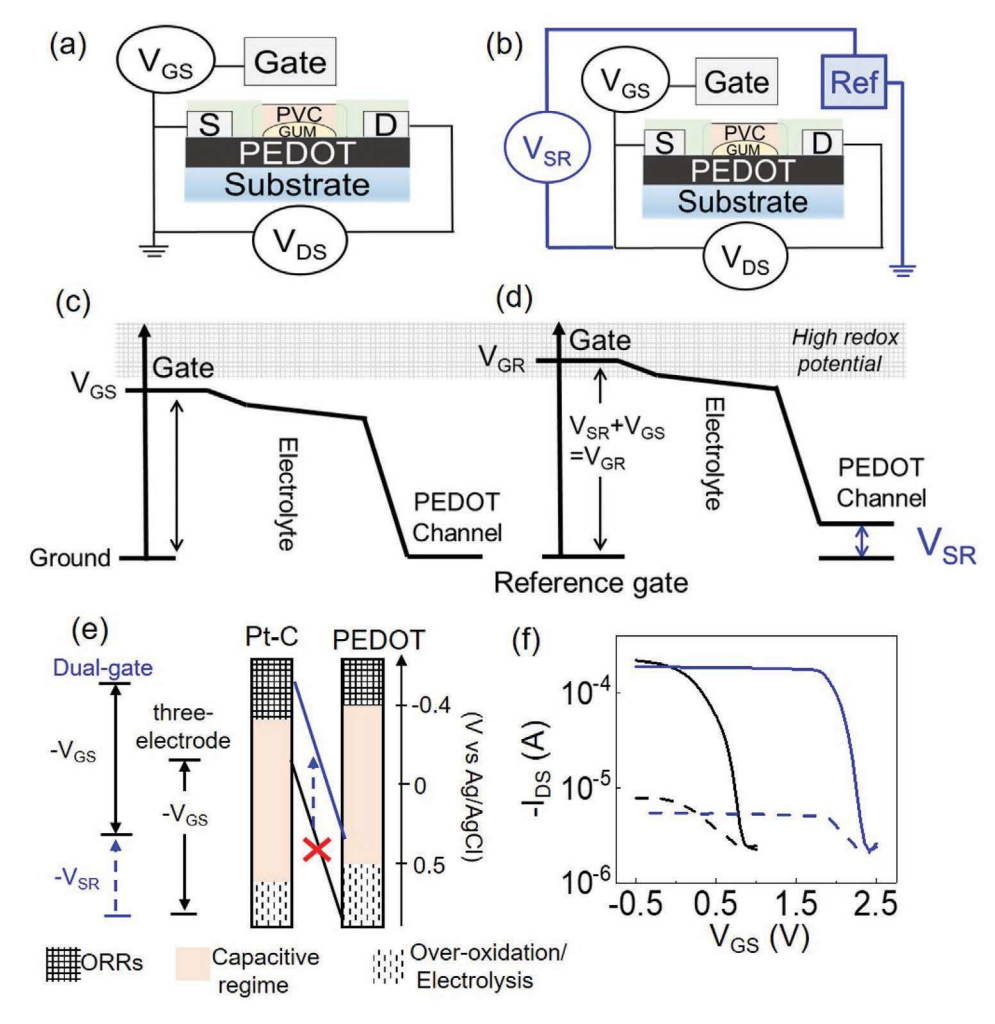


Figure 1. Schematics of a) the conventional three-electrode OECT and b) the dual-gate OECT with four electrodes. Voltage diagrams of the potential drop between a gate electrode and the channel in c) a conventional OECT and d) a dual-gate OECT. e) Electrochemical potential diagrams for the Pt-C gate and the PEDOT channel, comparing the dual-gate and conventional configurations. f) Transfer characteristics measured under the conventional three-electrode configuration (black data) and the dual-gate configuration (blue data) with $V_{SR} = -0.6$ V. The leakage currents ($V_{DS} = 0$ V) are shown as dashed lines.

and covered by a polyvinylchloride-based membrane. The gel electrolyte increased the current modulation and response speed. [15,27,28] The structure of our dual-gate OECT is shown in Figure 1b. The two gate electrodes were fabricated using a conductive carbon cloth. One of the electrodes was coated with a small amount of electrodeposited platinum to catalyze the ORRs. [29] The other gate electrode was coated with activated carbon (AcC) and served as the ground reference point. The voltage subscripts denote the electrode onto which a voltage was applied, with respect to another electrode. For example, $V_{\rm GS}$ is the voltage applied onto the Pt-C gate with respect to the source; $V_{\rm SR}$ is the voltage applied onto the source with respect to the AcC reference gate. The transistor channel region and the gates are exposed to the seawater while the source/drain contacts and interconnects are encapsulated in silicone.

For a conventional OECT, the source electrode is grounded and the channel is near the ground potential as shown in Figure 1c. The potential difference between the gate and source electrodes $V_{\rm GS}$ modulates the PEDOT channel to change drainsource current $I_{\rm DS}$. It is desirable to keep the channel operating within capacitive region and avoid irreversible over-oxidation at the channel. To meet this requirement, the range of $V_{\rm GS}$ is limited and not sufficient to activate ORRs at the Pt-C gate.

To reach the potential needed for ORRs, our novel dual-gate configuration includes an additional gate electrode as the ground reference (Figure 1d). The applied potential between the source electrode and this new reference $V_{\rm SR}$ will shift the voltages at the channel and at the Pt-C electrode, as illustrated in Figure 1e. The sum of $V_{\rm GS}$ and $V_{\rm SR}$ is the voltage difference $V_{\rm GR}$ between the Pt-C and AcC gates ($V_{\rm GR} = V_{\rm GS} + V_{\rm SR}$). Through controlling $V_{\rm SR}$, high redox potential reactions such as ORRs can be activated at the Pt-C gate; meanwhile, the PEDOT channel stays within the capacitive modulation window, away from undesirable Faradaic reactions. In contrast, the conventional three-electrode OECT is restricted to assigning the channel to near the ground level ($V_{\rm S} = 0$ V), thus exposing the semiconductor to Faradaic reactions that lead to degradation.

Our devices operated in depletion mode, in which a positive $V_{\rm GS}$ induced cations to migrate inside the semiconducting film and de-dope PEDOT, reducing its conductance. Transfer characteristics of the OECTs are shown in Figure 1f, with the transconductance and output characteristics included in Figure S1 (Supporting Information).

When the source electrode was grounded ($V_{SR} = 0$ V), our four-electrode structure effectively reverted to the conventional three-electrode configuration with a typical transfer characteristic displayed as the black line in Figure 1f. In the fourelectrode configuration with an additional reference gate, the source electrode was not constrained to the ground potential. By applying a voltage on the source electrode with respect to the reference electrode ($V_{SR} \neq 0$ V), the channel potential was shifted as illustrated in Figure 1d,e, effectively changing the device threshold voltage $V_{\rm T}$. For $V_{\rm SR} = -0.6$ V, the transfer characteristics denoted by the blue line in Figure 1f showed a V_T shift of 1.6 V compared to the conventional configuration. The carrier mobilities were derived to be ≈2 cm² V⁻¹ s⁻¹ and comparable between both configurations. The V_{SR} control here is similar to prior work that tuned V_T by back-channel gates^[30] or adjustment of electrochemical potentials at OECT gates.[31]

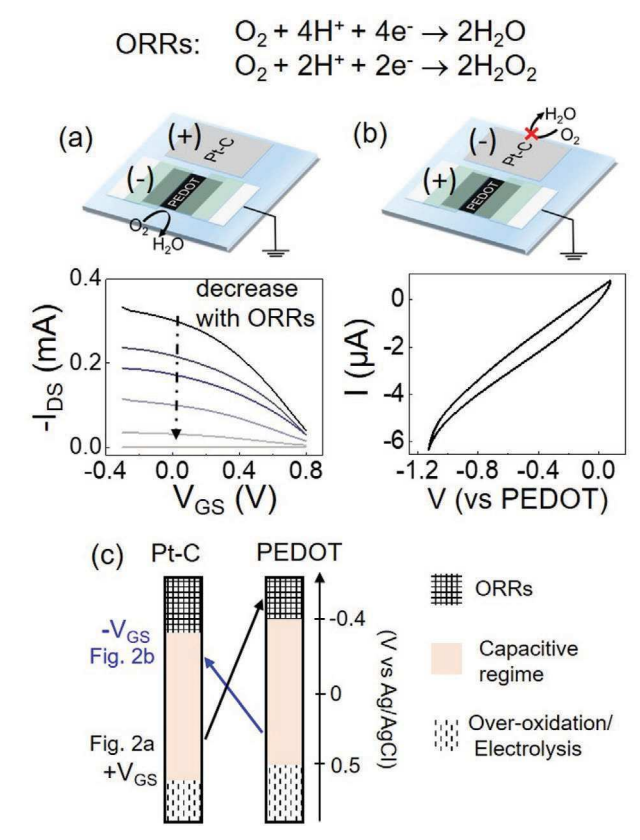


Figure 2. Issues encountered when using the conventional three-electrode OECT to measure dissolved oxygen through oxygen reduction reactions (ORRs). a) Transfer characteristics degraded by ORRs on the semiconductor. $V_{DS} = -0.2$ V. Each curve was measured after applying $V_{GS} = 0.8$ V for 200 s. b) ORRs not occurring on gate, as indicated by the low redox current. The drawings show the applied voltage polarity. The dissolved oxygen concentration was \approx 6 ppm. c) Electrochemical potential diagrams, illustrating PEDOT degradation due to ORRs (black line), or an insufficient potential to induce ORRs (blue line) as the Pt-C remained in nonreactive capacitive regime.

In addition to $V_{\rm T}$ tuning, our work applied this $V_{\rm SR}$ control to extend the sensor stability window, while maintaining high carrier mobility to improve sensitivity.

Before delving further into the operation of dual-gate OECT sensors, Figure 2 depicts the issues confronting conventional three-electrode OECTs in dissolved oxygen measurements. When the device was operated with positive V_{GS} , ORRs took place at the channel and over-oxidized the PEDOT semiconductor.[32] The channel conductance is irreversibly degraded by ORRs to a very low current level in Figure 2a. If the device was operated with negative V_{GS} , hypothetically, ORRs would be located at the Pt-C gate electrode. However, in practice, ORRs did not occur, as evident from the very low micro-ampere current between the gate and PEDOT channel in Figure 2b. The reason was that the applied potential dropped largely at the channel rather than at the gate, due to the channel capacitance being much lower than the gate capacitance (capacitance measurements in Figure S2a, Supporting Information). The small voltage drop at the gate was insufficient to generate the ORRs (depicted in Figure S2b, Supporting Information). Figure 2c presents electrochemical potential diagrams that summarize

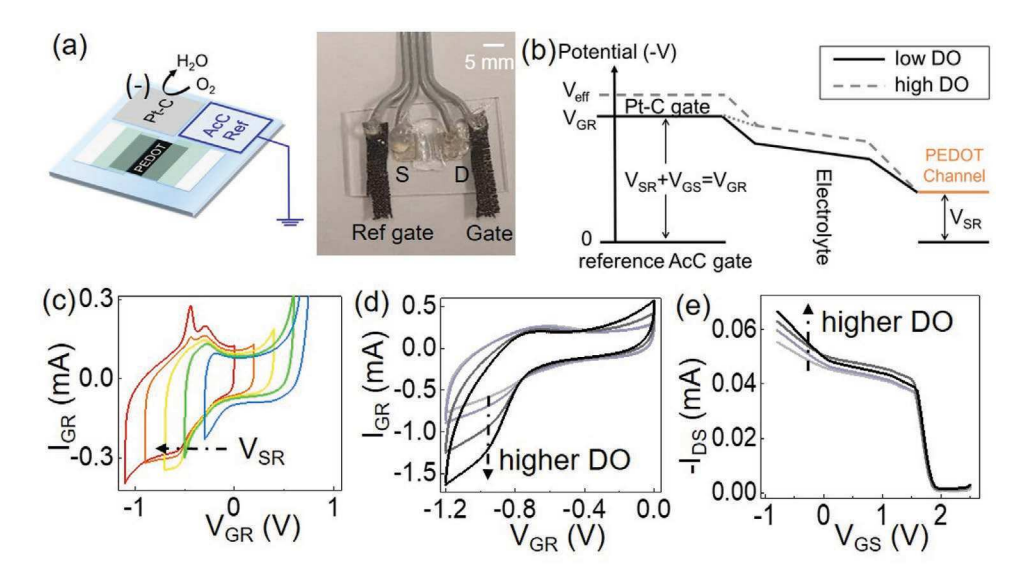


Figure 3. a) A schematic and a photograph of the dual-gate OECT. b) Voltage diagram for the OECT channel with respect to the two gates. The $V_{\rm eff}$ term is the effective bias on the channel, dependent on the analyte concentration. c) Current versus applied voltage between the Pt-C and activated carbon gates, as $V_{\rm CS}$ was scanned from -0.3 to 0.8 V. For each color, $V_{\rm SR}$ was changed in steps of -0.2 V starting at $V_{\rm SR} = 0$ V. d) Current versus voltage between gate electrodes. e) Transfer characteristics as a function of the dissolved oxygen concentration set at 1.5, 3, 6, or 8.5 ppm. Here, $V_{\rm DS} = -0.2$ V and $V_{\rm SR} = -0.6$ V.

the instability and limited potential range in conventional three-electrode OECTs. The gate and channel dimensions can be adjusted to increase the gate potential;^[33] but by comparison, the dual-gate structure would enable a more direct and simple approach to deliver a large potential that drives ORRs.

Figure 3a presents the schematic and a photograph of the dual-gate configuration. High redox potential reactions, such as ORRs, were activated by controlling the V_{GR} . The channel potential can be placed at a level between the gates, as illustrated by the orange level set by $V_{\rm SR}$ in Figure 3b. While the applied voltages $V_{\rm GS}$ and $V_{\rm SR}$ are independently adjustable, they add up to $V_{\rm GR}$ which determines whether the Pt-C electrode would undergo ORRs. In Figure 3c, the measured current I_{GR} between the gates increased with more negative V_{SR} , resulting in the onset of ORRs. Significant ORRs were generated starting at $V_{GR} = -0.8$ V, as evident in Figure 3d where the I_{GR} current increased when oxygen gas was bubbled into the sample. In Figure 3e and subsequent plots, we showed the device set at $V_{\rm SR} = -0.6$ V, but this choice of voltage value was just an example. As long as the potential $V_{\rm GR}$ (= $V_{\rm GS}$ + $V_{\rm SR}$) between the two gate electrodes is more negative than $-0.8\ V$, any combination of $V_{GS} + V_{SR}$ can be used to induce ORRs.

The effect of V_{GS} and V_{SR} on the channel source–drain current I_{DS} can be expressed by the following relations

$$I_{\rm DS} = \frac{Wd}{L} \mu C^* \left(V_{\rm T} - V_{\rm eff} + \frac{1}{2} V_{\rm DS} \right) V_{\rm DS}$$
 (1)

$$V_{\rm eff} = -V_{\rm SR} + V_{\rm GS} \frac{(1+\beta)}{(1-\beta\gamma)} \gamma - \frac{kT}{ze} \frac{(1+\beta)(1+\gamma)}{(1-\beta\gamma)} \ln Q_{\rm r} + {\rm constant} \qquad (2)$$

where W is the channel width, d is the semiconductor thickness, L is the channel length, μ is the mobility, and C^* is the

volumetric capacitance. The $V_{\rm eff}$ term is the effective bias on the channel, with dependence on the applied voltage levels $V_{\rm GS}$ and $V_{\rm SR}$ and the Faradaic reaction quotient $Q_{\rm r}$ that is proportional to the analyte concentration. The increase in $V_{\rm eff}$ with higher analyte concentration is illustrated in Figure 3b. The coefficient $\beta = C_{\rm PEDOT}/C_{\rm AcC}$ is the capacitance ratio of the PEDOT channel to the AcC reference gate, and $\gamma = C_{\rm Pt-C}/C_{\rm AcC}$ is the capacitance ratio of the Pt-C gate to the AcC reference gate. The parameter T is the temperature, k is the Boltzmann constant, e is the electron charge, and e is the number of electrons transferred in the redox reaction. The derivation of Equation (2) was built upon refs. [34,35] and explained in detail in the Supporting Information. Experimental verification of the equations is demonstrated in Figure S3 (Supporting Information).

In Figure 3e, the measured $I_{\rm DS}$ rose with the dissolved oxygen level in transfer characteristics. This response originated from the third term in Equation (2), which was based on the Nernst equation and was a function of analyte concentration. Specifically, with higher dissolved oxygen concentration, more ORRs occurred, and in turn $V_{\rm eff}$ became more negative, increasing $I_{\rm DS}$.

As we did not want to degrade the Pt-C electrode over time, we kept the operation window within the potential range that did not show irreversible reactions at Pt-C. The lower and upper potential limits of $V_{\rm GR}$ were observed to be $-1.2~{\rm V} < V_{\rm GR} < 0.6~{\rm V}$, as shown in Figure 3c,d. We did not test negative potential beyond $-1.2~{\rm V}$, and for positive potential above 0.6 V, there were irreversible reactions as seen in Figure 3c. To keep the PEDOT channel in the stable capacitive regime, the potential range was $-0.4~{\rm V} < V_{\rm GS} < 0.5~{\rm V}$, a safe potential window for a conventional three-electrode OECT. In comparison, the dual-gate OECT widened the potential window by $-0.8~{\rm V}$ in the negative potential range. For example, by applying $V_{\rm SR}$ of $-0.8~{\rm V}$ and $V_{\rm GS}$ at $-0.3~{\rm V}$, the PEDOT channel stays in the safe



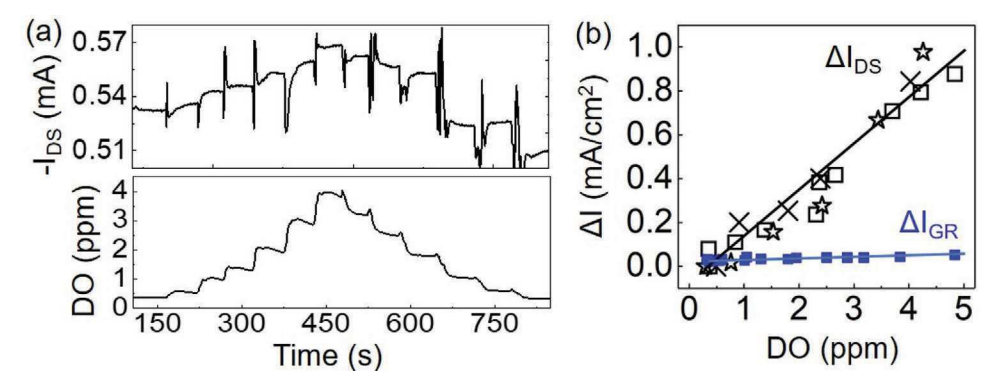


Figure 4. a) Top: source–drain current of the dual-gate OECT in seawater, as the dissolved oxygen concentration was varied. Bottom: corresponding measurement by the commercial calibration probe (Hanna model #HI98194). b) Sensor calibration curve measured at $V_{GS} = -0.3$ V, $V_{SR} = -0.6$ V, and $V_{DS} = -0.2$ V for three different devices, each with a different symbol. The black and blue colors represent the I_{DS} (222 μA cm⁻² ppm⁻¹) and I_{GR} (5.7 μA cm⁻² ppm⁻¹) responses, respectively.

capacitive regime, while $V_{\rm GR} = V_{\rm GS} + V_{\rm SR} = -1.1$ V, reaching a sufficiently high potential to induce ORRs.

2.2. Application of Dual-Gate OECTs to Monitor Dissolved Oxygen in Seawater

The device response to dissolved oxygen concentration was further calibrated at fixed gate voltages. We applied $V_{SR} = -0.6$ V to keep the PEDOT channel below the ORRs onset potential and prevent over-oxidation in the semiconductor; $V_{GS} = -0.3$ V was used to bring the total potential on the Pt-C gate to $V_{\rm GR}$ = -0.9 V, to induce ORRs that modulated the source-drain current. Figure 4a shows the dual-gate OECT response as a function of dissolved oxygen concentrations over time. The oxygenation level of the seawater sample was concurrently monitored by a commercial meter (Hanna model #HI98194) and was varied between 0.3 to 4 parts per million (ppm) by bubbling oxygen or nitrogen gas into the seawater. Figure 4b presents the OECT source-drain current versus dissolved oxygen concentration, and the ratio of current to analyte concentration determines the device sensitivity. The average sensitivity of the three devices is 222 µA cm⁻² ppm⁻¹, with deviations of $\pm 12\%$. We reported the current change with the baseline current subtracted $[\Delta I = I(x \text{ ppm}) - I(0 \text{ ppm})].$ The detection threshold was measured to be 0.3 ppm, and the sensors showed super-Nernstian sensitivity higher than prior thin-film electrochemical sensors (Table S1, Supporting Information). In other types of sensors, [2] such as fluorescence quenching or switchable-trace-amount oxygen sensors, the readouts are amplified by integrated circuits and reached lower detection limits than our device but at the expense of large device volume.

It is noted that the gate current $I_{\rm GR}$ in our devices was equivalent to the current readout in other oxygen sensors based on conventional cyclic voltammetry. [36] At its maximum the $I_{\rm GR}$ response was only 5.7 μ A cm⁻² ppm⁻¹, as shown in Figure S4 (Supporting Information). By comparison, the source–drain current $I_{\rm DS}$ sensitivity was 38 times better than the $I_{\rm GR}$ response, thus showcasing the benefit of channel modulation that enabled signal amplification in OECTs.

The dimensions of our OECT dissolved oxygen sensor are much more compact and less intrusive than typical electrochemical probes, and the OECT sensor provided local measurements within confined environments such as amid a saltwater green macro-algae (Chaetomorpha Chaeto) in Figure 5a. Macroalgae are prevalent in reef environments, and they are also grown in aquariums for water purification or to develop a sustainable energy source substitute for fossil fuels. [21,22] Photosynthesis in macro-algae is triggered by light and produces oxygen. Figure 5b demonstrates that our OECT sensor was able to monitor real-time changes of the dissolved oxygen level, as evidenced by the increased oxygen concentration upon light exposure of the macro-algae. Light sensitivity of device was less than 0.27% change in current upon illumination, and therefore light response was negligible and the sensor response was due to oxygen level change. The OECT signal correlated with corresponding measurements made using a commercial probe; the slight discrepancy might be due to the slower speed of the OECT (17.7 s settling time, Figure S5, Supporting Information) and different sensor locations. The commercial probe was farther away from the macro-algae than the OECT, and the oxygen concentration gradient at the probe location was more pronounced and possibly contributed to the dips in its signal, compared to the OECT sitting amid the oxygen-producing algae.

In addition, we measured the effect of pH changes on the oxygen sensor. The OECT $I_{\rm DS}$ showed less than a 0.7% change when pH was adjusted between 6 and 9 (broader than the typical pH range in the ocean) in Figure S6 (Supporting Information). Given that the $I_{\rm DS}$ current changed by 10% ppm⁻¹ of dissolved oxygen (Figure 5b), our OECT sensor was more sensitive to dissolved oxygen than pH changes, indicating that our devices exhibited specificity to the intended analyte.

We characterized the stability of a dual-gate OECT submerged in seawater over five days. The dissolved oxygen concentration of the seawater was periodically adjusted between 0 and 1 ppm, as shown in Figure 5c. The sensor response in Figure 5d clearly distinguished the two levels. As a proof of concept, the OECT dissolved oxygen sensor has demonstrated stable operation in seawater for 5 d. A caution is that the settling time in Figure 5c was much slower than in Figure 4a, because there was no stirring in the experiment and the settling



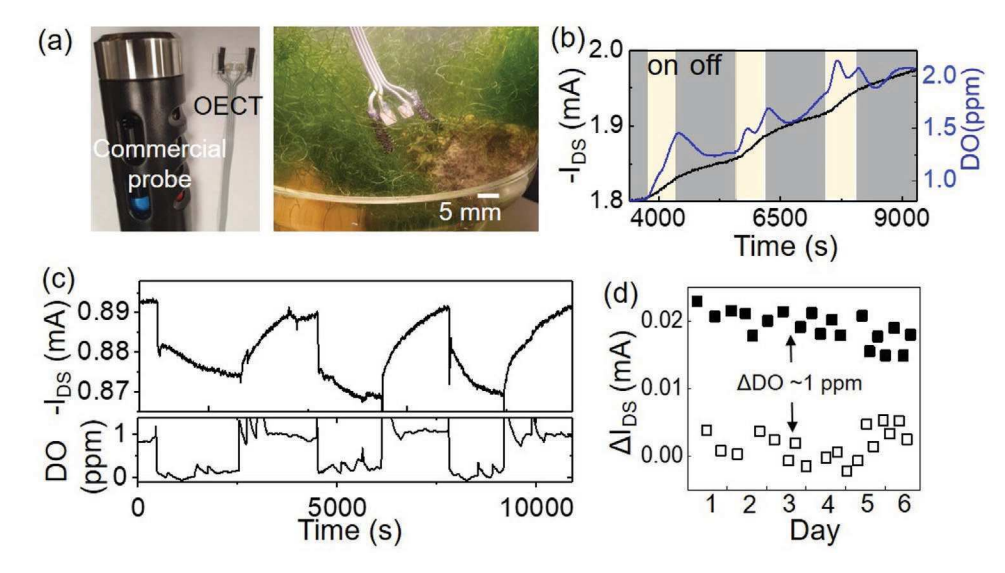


Figure 5. a) Photographs showing the compact form factor of our dual-gate OECT, which allowed non-intrusive sensing amid dense macro-algae. b) Monitoring changes in dissolved oxygen concentration as light triggered photosynthesis in the macro-algae. Black: OECT response, at $V_{\rm CS} = -0.3$ V, $V_{\rm SR} = -0.6$ V, and $V_{\rm DS} = -0.2$ V; blue: measurement by a commercial probe (Hanna model #HI98194). c) Comparison of the OECT response to the commercial probe output, as the dissolved oxygen concentration was tuned by bubbling gases into the sample tank. d) Extension of the measurements in (c) to check the sensor stability over 5 d, with the seawater periodically adjusted between oxygenation levels of 0 and 1 ppm.

time increased as the DO level decreased due to slow diffusion. The device was robust to electrostatic discharge (Figure S7, Supporting Information) often encountered in field operations. As a proof of concept, the OECT dissolved oxygen sensor has demonstrated stable operation in seawater for 5 d. Future studies will examine and improve the device stability further toward long-term operation, but the current lifetime is sufficient to meet the needs of short-term marine research.

3. Conclusions

The dual-gate configuration in this work provides a simple but effective approach to extend the electrochemical stability window of OECTs. This new device design allows large potential between the gates to facilitate sensing reactions, while modulating the channel within a lower potential range to maintain the semiconductor stability. We presented the analytical expressions for the current modulation in dual-gate OECTs. Complementary to the search for new channel materials to improve stability, the dual-gate strategy is applicable to existing semiconductors and simple to implement just by including an additional electrode. Thus, this work enables the use of conventional PEDOT materials in the challenging task of ORRs detection in marine environment.

As a miniaturized in situ sensor, the dual-gate OECT showed a detection limit of 0.3 ppm dissolved oxygen concentration in seawater. Below 5 ppm, the sensitivity was 222 $\mu A~cm^{-2}~ppm^{-1}.$ The device was capable of monitoring oxygenation changes due to saltwater macro-algae^[21,22] under photosynthesis cycles. Signal drift and interference by pH changes were characterized, and the OECT dissolved oxygen sensor has demonstrated stable operation in seawater for over 5 d. In addition to monitoring dissolved oxygen, the dual-gate OECT sensor can be extended to other analytes, to reduce the size, weight, and cost

of sensor systems and enable non-intrusive studies of marine ecosystems.

4. Experimental Section

Xanthan Gum Electrolyte and Polyvinylchloride (PVC)-Based Membrane Preparation: The chemicals were purchased from Sigma-Aldrich and used as received, unless noted otherwise. The xanthan gum electrolyte was prepared by dissolving 5 g xanthan gum powder in 50 mL of 1 m sodium sulfate aqueous solution. [26] The PVC-based cocktail membrane was prepared based on a formulation in ref. [37] but excluding the hydrogen ionophore. The mixture consisted of 1 mL tetrahydrofuran, 59 mg of 2-nitrophenyl octyl ether, 29.5 mg of PVC, 0.44 mg of sodium tetrakis [3,5-bis (trifluoromethyl) phenyl]borate, and 10.3 mg of tetrakis (4-chlorophenyl)borate tetradodecyl-ammonium salt (ETH 500). The solution was drop-cast onto a glass slide and allowed to dry over a day, to form stand-alone thin films that would be transferred onto OECT channels.

OECTs Fabrication: Glass substrates were cleaned by sonication in isopropanol and then in acetone. Kapton tapes were used as stencil masks to define the channel and electrode dimensions. PEDOT:PSS (Clevios P1000) was spin-coated onto the mask-covered substrate at 2000 rpm. After removing the stencil mask, the PEDOT:PSS film was annealed at 120 °C for 30 min. Subsequently, the film was immersed in concentrated sulfuric acid for 15 min to remove PSS,[23] followed by rinsing with deionized water for three times to remove the residual acid. Silver/silver chloride ink (Ercon part #E2414) was deposited[38] onto the PEDOT film to define source and drain electrodes. Silicone (Ecoflex) was stencil printed to encapsulate the electrodes and define the channel dimensions to be 1 cm in width and 0.2 cm in length. After the silicone has completed crosslinking, the xanthan gum electrolyte was drop-cast onto the defined channel area. A piece of the PVC-based membrane was placed over the channel area and pressed onto the electrolyte. Finally, silicone was applied again to seal the membrane edge.

For ORRs catalysis, the Pt-C gate electrode was fabricated by electrodepositing a small amount of platinum on the conductive carbon cloth (AvCarb MGL190). A commercial Pt carbon cloth (FuelCellStore,



www.advancedsciencenews.com



0.3 mg cm $^{-2}$ 40% Pt) was used as the Pt source. It served as the working electrode to which potential cycles were applied versus Ag/AgCl, and the carbon cloth was the counter electrode. The potential cycles were swept from 1.2 to 0.8 V for 30 times in aqueous electrolyte made from Instant Ocean, and Pt was found to be incorporated into the counter carbon cloth electrode. [39] For the reference electrode, AcC was selected because it was more stable than Ag/AgCl in marine environments. The AcC slurry was prepared by mixing activated carbon powder (Kuraray Chemical, YP50F) and polyvinylidene fluoride binder at 9:1 weight ratio. The mixture was added to N-methyl-2-pyrrolidone solvent to reach 60–70% solid content by weight. Then, the slurry was evenly deposited onto the carbon cloth and annealed at 80 °C for 1 h. The two gate electrodes were attached adjacent to the PEDOT channel to complete the OECT. The gate electrode dimensions were 1 cm \times 0.5 cm.

Electrochemical Characterization: Cyclic voltammetry and electrochemical impedance spectroscopy were carried out using a potentiostat (BioLogic SP-200) to measure devices submerged in artificial seawater (Instant Ocean sea salt) or ocean samples from La Jolla Cove in San Diego (Figure S8, Supporting Information). OECT measurements were taken with electrometers (Keithley 2000) controlled by LabVIEW software. The concentration of dissolved oxygen was adjusted by purging oxygen or nitrogen through the seawater and monitored by an oxygen meter (Hanna model #HI98194) in real time.

The light source used in the photosynthesis experiment was from a 20 W fluorescent compact light bulb with color temperature of 5000 K. During the course of this measurement, the temperature and pH of the seawater tank were monitored and changed by at most 3.5%, and the light sensitivity of device was less than 0.27% change in current upon illumination (Figure S9, Supporting Information). Thus these factors had negligible effect on the oxygen sensor signal. To understand the device stability^[40] over 5 d, the electrode voltages were submerged in the seawater sample over 144 h, and the biases were switched on only during measurements. The water tank setup was shown in Figure S10 (Supporting Information).

Supporting Information

Supporting Information is available from the Wiley Online Library or from the author.

Acknowledgements

The authors want to thank Jeonghyun Ahn and Yichen Zhai for carrying out experiments of electrostatic discharge on OECTs. This project was supported by Office of Naval Research award N00014-19-1-2687.

Conflict of Interest

The authors declare no conflict of interest.

Author Contributions

S.W. and T.N.N. designed and analyzed the experiments and wrote the manuscript. A.B., A.S., J.A., and T.N.N. planned the oxygen sensor specifications. S.W. carried out the fabrication and measurements.

Data Availability Statement

The data that support the findings of this study are available from the corresponding author upon reasonable request.

Keywords

dissolved oxygen sensors, electrochemical stability, marine sensors, organic electrochemical transistors

Received: March 4, 2021 Published online:

- [1] D. Breitburg, L. A. Levin, A. Oschlies, M. Grégoire, F. P. Chavez, D. J. Conley, V. Garçon, D. Gilbert, D. Gutiérrez, K. Isensee, G. S. Jacinto, K. E. Limburg, I. Montes, S. W. A. Naqvi, G. C. Pitcher, N. N. Rabalais, M. R. Roman, K. A. Rose, B. A. Seibel, M. Telszewski, M. Yasuhara, J. Zhang, Science 2018, 359, 46.
- [2] Y. Wei, Y. Jiao, D. An, D. Li, W. Li, Q. Wei, Sensors 2019, 19, 3995.
- [3] X. Guimer, A. Moya, A. D. Dorado, X. Illa, R. Villa, D. Gabriel, X. Gamisan, G. Gabriel, Sensors 2019, 19, 4747.
- [4] Y. G. Kim, Y. J. Tak, H. J. Kim, W. G. Kim, H. Yoo, H. J. Kim, Sci. Rep. 2018, 8, 5546.
- [5] M. Amit, R. K. Mishra, Q. Hoang, A. M. Galan, J. Wang, T. N. Ng, Mater. Horiz. 2019, 6, 604.
- [6] C. Bao, W. S. Kim, Adv. Eng. Mater. 2020, 22, 2000116.
- [7] J. M. Nassar, S. M. Khan, S. J. Velling, A. Diaz-Gaxiola, S. F. Shaikh, N. R. Geraldi, G. A. Torres Sevilla, C. M. Duarte, M. M. Hussain, NPI Flexible Electron. 2018, 2, 13.
- [8] E. MacChia, R. A. Picca, K. Manoli, C. Di Franco, D. Blasi, L. Sarcina, N. Ditaranto, N. Cioffi, R. Österbacka, G. Scamarcio, F. Torricelli, L. Torsi, *Mater. Horiz.* 2020, 7, 999.
- [9] J. Rivnay, S. Inal, A. Salleo, R. M. Owens, M. Berggren, G. G. Malliaras, Nat. Rev. Mater. 2018, 3, 17086.
- [10] O. Parlak, S. T. Keene, A. Marais, V. F. Curto, A. Salleo, Sci. Adv. 2018, 4, eaar2904.
- [11] C. H. Mak, C. Liao, Y. Fu, M. Zhang, C. Y. Tang, Y. H. Tsang, H. L. W. Chan, F. Yan, J. Mater. Chem. C 2015, 3, 6532.
- [12] X. Xi, D. Wu, W. Ji, S. Zhang, W. Tang, Y. Su, X. Guo, R. Liu, Adv. Funct. Mater. 2020, 30, 1905361.
- [13] E. Macchia, P. Romele, K. Manoli, M. Ghittorelli, M. Magliulo, Z. M. Kovács-Vajna, F. Torricelli, L. Torsi, Flexible Printed Electron. 2018, 3, 034002.
- [14] S. Wustoni, C. Combe, D. Ohayon, M. H. Akhtar, I. McCulloch, S. Inal, Adv. Funct. Mater. 2019, 29, 1904403.
- [15] M. Sessolo, J. Rivnay, E. Bandiello, G. G. Malliaras, H. J. Bolink, Adv. Mater. 2014, 26, 4803.
- [16] V. Gueskine, A. Singh, M. Vagin, X. Crispin, I. Zozoulenko, J. Phys. Chem. C 2020, 124, 13263.
- [17] P. Kumar, Z. Yi, S. Zhang, A. Sekar, F. Soavi, F. Cicoira, Appl. Phys. Lett. 2015, 107, 6.
- [18] A. Giovannitti, R. B. Rashid, Q. Thiburce, B. D. Paulsen, C. Cendra, K. Thorley, D. Moia, J. T. Mefford, D. Hanifi, D. Weiyuan, M. Moser, A. Salleo, J. Nelson, I. McCulloch, J. Rivnay, Adv. Mater. 2020, 32, 1908047.
- [19] A. F. Paterson, A. Savva, S. Wustoni, L. Tsetseris, B. D. Paulsen, H. Faber, A. H. Emwas, X. Chen, G. Nikiforidis, T. C. Hidalgo, M. Moser, I. P. Maria, J. Rivnay, I. McCulloch, T. D. Anthopoulos, S. Inal, Nat. Commun. 2020, 11, 3004.
- [20] K. Wang, L. Huang, N. Eedugurala, S. Zhang, M. A. Sabuj, N. Rai, X. Gu, J. D. Azoulay, T. N. Ng, Adv. Energy Mater. 2019, 1902806.
- [21] F. Fernand, A. Israel, J. Skjermo, T. Wichard, K. R. Timmermans, A. Golberg, Renewable Sustainable Energy Rev. 2017, 75, 35.
- [22] S. Abu-Ghosh, D. Fixler, Z. Dubinsky, D. Iluz, *Bioresour. Technol.* 2016, 203, 357.
- [23] N. Kim, S. Kee, S. H. Lee, B. H. Lee, Y. H. Kahng, Y.-R. R. Jo, B.-J. J. Kim, K. Lee, Adv. Mater. 2014, 26, 2268.



www.advancedsciencenews.com



- [24] S. M. Kim, C. H. Kim, Y. Kim, N. Kim, W. J. Lee, E. H. Lee, D. Kim, S. Park, K. Lee, J. Rivnay, M. H. Yoon, *Nat. Commun.* 2018, 9, 3858.
- [25] K. Wang, L. Yao, M. Jahon, J. Liu, M. Gonzalez, P. Liu, V. Leung, X. Zhang, T. N. Ng, ACS Energy Lett. 2020, 5, 3276.
- [26] N. Yu, X. Wang, S. Zhang, S. Zeng, Y. Zhang, J. Di, Q. Li, RSC Adv. 2019, 9, 8169.
- [27] C. G. Bischak, L. Q. Flagg, D. S. Ginger, Adv. Mater. 2020, 32, 202002610.
- [28] V. Kaphle, S. Liu, C. M. Keum, B. Lüssem, Phys. Status Solidi A 2018, 215, 1800631.
- [29] K. B. Liew, W. R. W. Daud, M. Ghasemi, J. X. Leong, S. S. Lim, M. Ismail, Int. J. Hydrogen Energy 2014, 39, 4870.
- [30] M. Spijkman, E. C. P. Smits, P. W. M. Blom, D. M. de Leeuw, Y. Bon Saint Côme, S. Setayesh, E. Cantatore, Appl. Phys. Lett. 2008, 92, 143304.
- [31] S. E. Doris, A. Pierre, R. A. Street, Adv. Mater. 2018, 30, 1706757.

- [32] J. Fan, S. S. Rezaie, M. Facchini-Rakovich, D. Gudi, C. Montemagno, M. Gupta, Org. Electron. 2019, 66, 148.
- [33] F. Cicoira, M. Sessolo, O. Yaghmazadeh, J. A. Defranco, S. Y. Yang, G. C. Malliaras, Adv. Mater. 2010, 22, 1012.
- [34] D. A. Bernards, D. J. MacAya, M. Nikolou, J. A. Defranco, S. Takamatsu, G. G. Malliaras, J. Mater. Chem. 2008, 18, 116.
- [35] J. T. Friedlein, R. R. McLeod, J. Rivnay, Org. Electron. 2018, 63, 398.
- [36] A. Moya, E. Sowade, F. J. del Campo, K. Y. Mitra, E. Ramon, R. Villa, R. R. Baumann, G. Gabriel, Org. Electron. 2016, 39, 168.
- [37] P. Kraikaew, S. Jeanneret, Y. Soda, T. Cherubini, E. Bakker, ACS Appl. Mater. Interfaces 2020, 5, 650.
- [38] Y. Zhai, Z. Wang, K. S. Kwon, S. Cai, D. Lipomi, T. N. Ng, Adv. Mater. 2020, 2002541.
- [39] P. J. Ferreira, G. J. la O', Y. Shao-Horn, D. Morgan, R. Makharia, S. Kocha, H. A. Gasteiger, J. Electrochem. Soc. 2005, 152, A2256.
- [40] T. N. Ng, M. L. Chabinyc, R. A. Street, A. Salleo, presented at IEEE Int. Reliability Physics Symp., Phoenix, AZ, September 2007, pp. 243–247.